This manuscript is in review at IEEE Geoscience and Remote Sensing Letters.

Julie Z. Miller
EarthSAR, LLC
jzmiller@earthsar.com

David .G Long
Department of Electrical and Computer Engineering
Brigham Young University

Riley Culberg
Department of Earth and Atmospeheric Sciences
Cornell University

Joel Harper
Department of Geosciences
University of Montana

Mapping Ice Slabs over Antarctic Ice Shelves using Quad-Polarization L-band Radar Backscatter

Julie Z. Miller, *Member, IEEE,* David G. Long, *Life Fellow, IEEE,* Riley Culberg, *Member, IEEE,* Joel Harper

***Abstract*—Nearly 3 months of enhanced-resolution, quad-polarization, L-band (1.26 GHz) radar backscatter (σ^o) image time series are used to map the ice slab extent over the percolation facies of Antarctic ice shelves for the first time from space. Distinctive spatial trends in σ^o, incidence angle, and polarization signatures mapped via principal component analysis (PCA) are used to develop a proof-of-concept polarimetric algorithm that is empirically calibrated using airborne ice-penetrating radar surveys. A previously unidentified ice slab extent of ~52,000 km^2 is mapped over 23 ice shelves in the Antarctic Peninsula as well as West and East Antarctica in locations that experience $\geq$35 days of surface melting during the austral melting season.**

***Index Terms*—SMAP, radar scatterometry, radar polarimetry, radar backscatter, Antarctica, ice shelf hydrology, ice slabs.**

I. INTRODUCTION

METERS-THICK ice slabs form as a sub-facies of the percolation facies of polar ice sheets [1] and span spatial scales of tens to hundreds of square kilometers [2], [3], [4], [5], [6], [7]. In the percolation facies, seasonal meltwater is typically retained in a firn column with ample storage capacity [8]. Meltwater vertically and heterogeneously infiltrates and refreezes as embedded ice structures that incorporate sequences of thinner ice layers interspersed with networks of ice pipes and ice lenses [8], [9]. However, widespread ice slab formation and expansion can rapidly occur during successive, intense and sometimes record-breaking, melting seasons that commonly include rainfall [2], [3], [4], [6] and are often associated with atmospheric rivers [10] and heat domes [11]. Heavy rainfall events can also form or expand ice slabs during the freezing season [12]. Extensive meltwater and/or rainwater infiltration in the firn column (<20 m), pore space saturation, and refreezing amalgamate embedded ice structures and transition the upper firn column into a low-permeability, solid-ice layer overlying a deeper, permeable firn layer. Ice slabs effectively seal off percolation facies subsurfaces [13].

Manuscript received X X, XXXX; revised X X, XXXX; accepted X X, XXXX. Date of publication X X, XXXX; date of current version X X, XXXX. This research was supported by the NASA Cryospheric Sciences Program (80NSSC21K0749) and the NASA SMAP Science Team (80NSSC20K1806). (*Corresponding author: J. Z. Miller.*)

J. Z. Miller is with EarthSAR, LLC, Salt Lake City, Utah 84117 USA and the Earth Science and Observation Center, Cooperative Institute for Research in Environmental Sciences, University of Colorado, Boulder, Colorado 80309 USA (e-mail: jzmiller@earthsar.com).

D. G. Long is with the Department of Electrical and Computer Engineering, Brigham Young University, Provo, Utah 84602 USA (e-mail: long@ee.byu.edu).

R. Culberg is with the Department of Earth and Atmospheric Sciences, Cornell University, Ithaca, New York 14853 USA (email: rtc84@cornell.edu).

J. Harper is with the Department of Geosciences, University of Montana, Missoula, Montana, 59812 USA (email: joel@mso.umt.edu).

Digital Object Identifier X/X

On the Greenland Ice Sheet, the ice slab extent over the percolation facies has been extensively mapped via firn cores [3], [4], [13], ground penetrating radar (GPR) transects [3], [4], airborne ice-penetrating radar surveys [4], [5], [6], [7], and satellite microwave remote sensing [5], [7]. However, on the Antarctic Ice Sheet, ice slabs have only been documented using firn cores and GPR transects at a single field site in Cabinet Inlet on Larsen C Ice Shelf, northern Antarctic Peninsula (see Fig. 1 for the location, red text) [2].

The objective of this exploratory study is to demonstrate the capability for mapping the ice slab extent over the percolation facies of Antarctic ice shelves for the first time from space using quad-polarimetric, L-band satellite radar scatterometry. As a result of technological advances and the recent launch of innovative, quad-polarimetric, satellite radar missions, radar polarimetry [14] is a powerful, emerging technique that enables continent-wide mapping of previously unidentified features over the Earth's surface—including ice slabs.

We use enhanced-resolution, quad-polarization, L-band (1.26 GHz) radar backscatter (σ^o) image time series [15]—the first-ever over Antarctica (e.g., see Fig. 1, false color composite)—generated using σ^o observations (2015) collected by the short-lived (83 days) radar aboard the NASA Soil Moisture Active Passive (SMAP) mission [16] (Section II-A) and the Scatterometer Image Reconstruction (SIR) algorithm [15] (Section II-B). Quad-polarization σ^o image time series facilitate analysis of polarization signatures resulting from Brewster angle effects [14] that occur at the smooth dielectric interfaces between ice slabs and firn layers. We develop a proof-of-concept polarimetric algorithm using distinctive spatial trends in σ^o, incidence angle, and polarization signatures mapped via principle component analysis (PCA) (Section II-C). We use: (1) airborne ice-penetrating radar surveys (2016-2018) collected by the Center for Remote Sensing of Ice Sheets (CReSIS) Accumulation Radar (AR) and Multi-Channel Coherent Radar Depth Sounder (MCoRDS3) flown as part of NASA Operation IceBridge (OIB) campaigns in the Antarctic Penisula [17] and (2) an Antarctic ice shelf mean surface melting days map (see [18] for a map description) derived from enhanced-resolution C-band (5.4 GHz) σ^o observations (2008-2015) collected by the ESA Advanced SCATterometer (ASCAT) mission [19] to empirically calibrate [5], [20] the proof-of-concept polarimetric algorithm (Section II-D).

II. MAPPING ICE SLABS OVER ANTARCTIC ICE SHELVES

A. Quad-Polarization L-band Radar Backscatter Observations

The SMAP mission [16] was launched on 31 January 2015 and began science operations on 31 March 2015. The state-

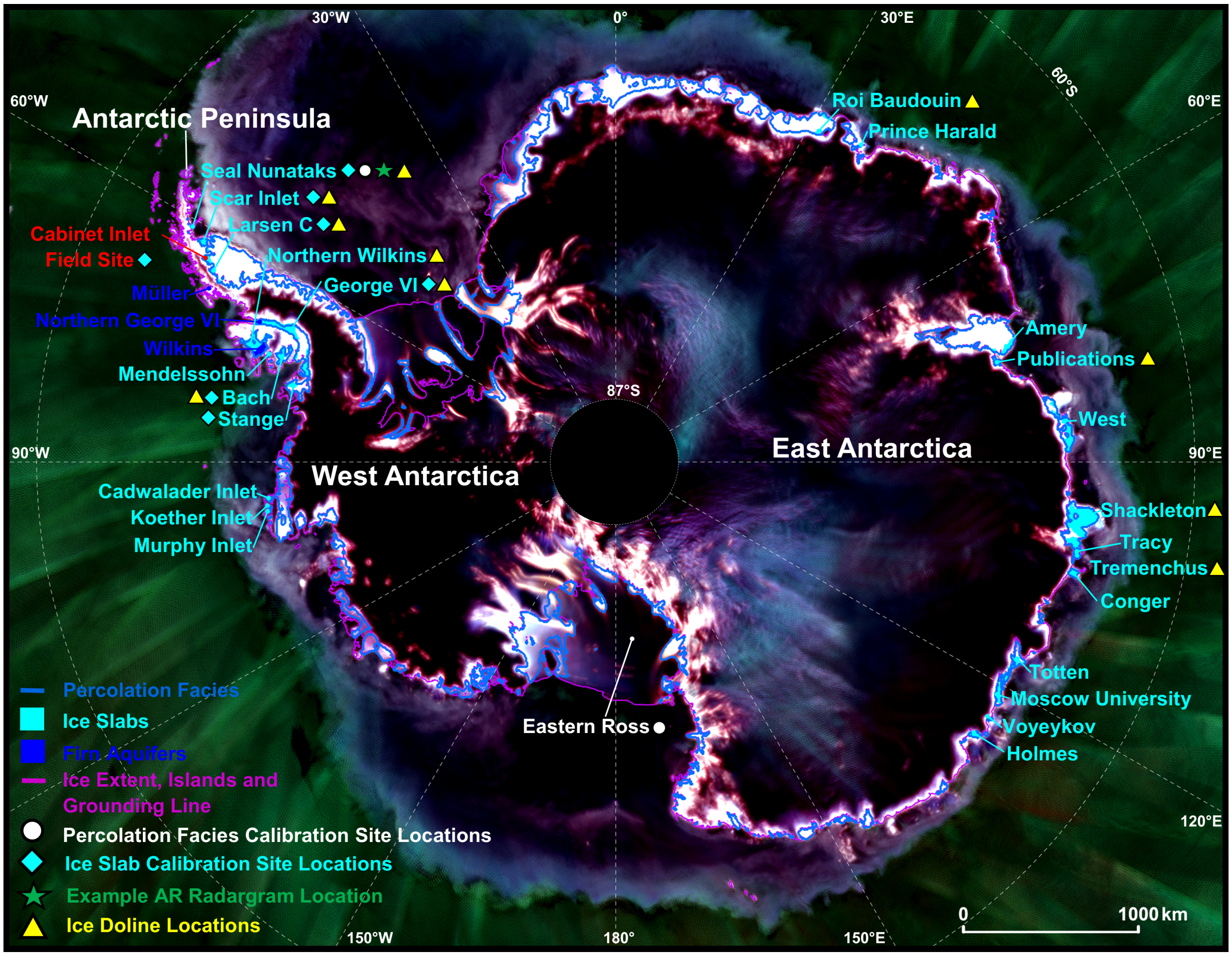

Fig. 1. Enhanced-resolution false color composite (red channel: A_{XX}[-39, -13 dB], green channel: A_{VV}[-20, -8 dB], and blue channel: A_{HH}[-25, -8 dB]) generated using scatterometer-mode σ^o observations collected by the radar aboard the SMAP mission during the evening satellite orbital pass over Antarctica over the 8-day imaging interval between 13-20 April 2015 (see Section II-A and II-B). The basemap is overlaid with the percolation facies (lighter blue lines), ice slab (cyan shading), and firn aquifer (darker blue shading) extents (see Sections II-C and II-D), the 2014 Mosaic of Antarctica ice extent, islands, and grounding lines (fuchsia lines) [21], the percolation facies (white circles) and ice slab (cyan diamonds) calibration site locations (see Section II-D), the example AR radargram location (see Fig. 2), and ice doline locations identified using Landsat high-resolution (15 m) panchromatic satellite imagery (yellow circles, see Sections III and IV). Note that ice slabs overlay the firn aquifer on the northern Wilkins Ice Shelf, Antarctic Peninsula [20].

of-the-art L-band instrument architecture integrates a quad-polarimetric radar and fully polarimetric radiometer. The radar stopped transmitting on 7 July 2015 as a result of a hardware anomaly, though the radiometer remains operational.

The 1.26 GHz radar is a conically-scanning, pencil-beam radar scatterometer capable of unfocused synthetic aperture radar (SAR) processing. It collected σ^o observations across the satellite's 1000 km swath in horizontal transmit/receive (σ^o_{HH}), vertical transmit/receive (σ^o_{VV}), horizontal transmit/vertical receive (σ^o_{HV}), and vertical transmit/horizontal receive (σ^o_{VH}) polarizations at a nominal surface incidence angle of 40°. In scatterometer-mode, on-board range-Doppler processing resolved the low-resolution (29×36 km) antenna footprint into 12 higher-resolution (6×30 km) slices (see the diagram in Fig. 3 of [15]). The radar also operated in high-resolution (1-3 km) SAR-mode. However, σ^o observations were only collected in scatterometer-mode over Antarctica and require image reconstruction to improve the effective resolution. The measurement accuracy is ∼1 dB for σ^o_{HH} and σ^o_{VV} observations and ∼1.5 dB for σ^o_{HV} and σ^o_{VH} observations [16].

B. Enhanced-Resolution A and B Image Time Series

The scatterometer-mode σ^o observations collected by the radar aboard the SMAP mission are reconstructed using the SIR algorithm [15]. The σ^o and the incidence angle (θ) variation are modeled using a linear equation defined by

$$\sigma^o = A + B(\theta - 40^\circ), \quad (1)$$

where A is the mean σ^o normalized to a 40° incidence angle (dB) and B is the slope in the σ^o versus the incidence angle (dB/°). The incidence angle ranges from 38° to 42°. A represents the sum of the volume and surface scattering components, which are influenced by the observation geometry, the polarization, and the geophysical and dielectric properties of the Earth's surface [14]. B represents the incidence angle variation related to volume and surface scattering [14] as well as angular, asymmetrical, and/or tilted features (see the diagram in Fig. 2 of [22]). Over Antarctica, the SIR algorithm separately combines σ^o observations collected during morning and evening satellite orbital passes between

00:00-12:00 and 12:00-24:00 local-time-of-day to generate enhanced-resolution, A and B images projected onto the Southern Hemisphere *EASE-Grid 2.0* at a 3.125 km grid cell spacing (e.g., see Fig. 1, false color composite). The effective resolution of the A and B images is ~5-10 km. [15].

We average the theoretically identical [14] single cross-polarized A (A_{HV} and A_{VH}) and B (B_{HV} and B_{VH}) images into combined cross-polarized A (A_{XX}) and B (B_{XX}) images to reduce the noise levels. The A (A_{HH}, A_{VV}, and A_{XX}) and B (B_{HH}, B_{VV}, and B_{XX}) image time series extend from the austral fall to early winter operational period of the radar (13 April 2015-05 July 2015) and alternate morning and evening satellite orbital passes. We construct Antarctic ice shelf masked (see [21] for a mask description) and concatenated A (Ψ_A = [A_{HH}, A_{VV}, A_{XX}]) and B (Ψ_B = [B_{HH}, B_{VV}, B_{XX}]) image arrays to use as the inputs into the PCA.

C. Principle Component Analysis

PCA is a well-known and widely applied multivariate statistical technique that linearly transforms large image arrays into smaller sets of uncorrelated images by geometrically projecting the image array into unitless dimensions termed principal components (PCs). The first PC represents the maximum percentage of the variance between the image array and its projection onto the PC. Subsequent orthogonal PCs account for decreasing maximum percentages of the remaining variance. We calculate the PCs of the Ψ_A and Ψ_B image arrays using a forward PC rotation and the eigenvectors of the covariance matrix. We limit the analysis to the first three PCs of the Ψ_A image array ($PC1\Psi_A$, $PC2\Psi_A$, $PC3\Psi_A$) and the first PC of the Ψ_B image array ($PC1\Psi_B$), which account for more than 90% of the respective cumulative variance.

1) $PC1\Psi_A$ and $PC1\Psi_B$: The first PCs of the Ψ_A and Ψ_B image arrays represent composite, quad-polarization, A and B images that have been denoised to remove instrument-based and image reconstruction artifacts. $PC1\Psi_A$ accounts for 99.5% of the variance and values range from -576 to -46. We use $PC1\Psi_A$ to map σ^o signatures. $PC1\Psi_B$ accounts for 91.1% of the variance and values range from -6 to 11. We use $PC1\Psi_B$ to map incidence angle signatures.

2) $PC2\Psi_A$: The spatial trends in $PC2\Psi_A$ are nearly identical to the spatial trends in $PC1\Psi_B$. $PC2\Psi_A$ accounts for 0.37% of the variance and values range from 54 to -93. Noting that the incidence angle variation is modeled using a linear equation that is not exact [15], we consider the variance to be a residual effect of the simplified modeling and therefore do not further consider $PC2\Psi_A$ in the polarimetric algorithm.

3) $PC3\Psi_A$: The third PC of the Ψ_A image array represents a composite, co- and cross-polarization ratio image (see Eqs. 10.16a and 10.16b in [14] for a description). It is critical for mapping ice slabs using the polarimetric algorithm. $PC3\Psi_A$ accounts for 0.04% of the variance and values range from -23 to 16. We use $PC3\Psi_A$ to map polarization signatures resulting from Brewster angle effects.

D. Empirical Calibration

1) Percolation Facies Extent: To empirically calibrate the polarimetric algorithm to map the percolation facies extent, we use $PC1\Psi_A$ over the eastern Ross Ice Shelf, West Antarctica and Seal Nunataks Ice Shelf, northern Antarctic Peninsula (see Fig. 1 for the locations, white circles). The eastern Ross Ice Shelf typically experiences negligible surface melting and can be characterized as dry snow facies [1]. We attribute low values over the dry snow facies ($PC1\Psi_A \in [-400, -300]$) to weak, depth-integrated, volume scattering in the firn column from individual snow grains, small (millimeter scale) relative to the L-band wavelength (24 cm), that attenuate electromagnetic energy [23], [24], [14]. This scattering mechanism decreases the net backscattering response. Contrastingly, Seal Nunataks Ice Shelf typically experiences intense, long-duration, surface melting and can be characterized as wet snow facies [1]. It has been inferred in previous studies to have a firn column that has at least partially transitioned into a meters-thick superimposed ice layer overlying deeper shelf-ice [25]. We attribute low values over the wet snow facies ($PC1\Psi_A \in [-576, -300]$) to both specular surface scattering from the smooth dielectric interfaces of the superimposed ice [23], [14] and diffuse surface scattering from the rough dielectric interfaces, such as expansive crevasse fields near grounding and shear zones, pressure ridges, flow-parallel longitudinal and traverse structures, partial-depth fractures, and full-shelf-ice-thickness rifts that reflect electromagnetic energy away from the radar's antenna [14]. These surface scattering mechanisms also decrease the net backscattering response.

We set a threshold of $PC1\Psi_A = -300$, which masks the dry and wet snow facies and maps a plausible percolation facies extent that is consistent with climatological surface melting trends. As previously noted, seasonal meltwater refreezes as sequences of thinner ice layers interspersed with networks of ice pipes and ice lenses [9] as well as meters-thick ice slabs [2], [3], [4]. Firn aquifers also form as a sub-facies of the percolation facies [5]. We attribute high values in the percolation facies ($PC1\Psi_A \in [-300, -46]$) to strong, depth-integrated, volume scattering in the firn column from ice pipes and ice lenses, large (tens of centimeters scale) relative to the L-band wavelength, that intensify electromagnetic energy returned to the radar's antenna and increase the net backscattering response [23], [26]. Specular surface scattering from the smooth dielectric interfaces, such as ice layers, ice slabs, and the upper surface of meltwater in firn aquifers, also contributes by decreasing the net backscattering response [14].

2) Ice Slab Extent: To empirically calibrate the polarimetric algorithm to map the ice slab extent, we combine $PC3\Psi_A$, $PC1\Psi_B$, and the mean surface melting days map [18] with the available airborne ice-penetrating radar surveys [17] collected over the mapped percolation facies extent in the Antarctic Peninsula. AR was flown aboard P3 (2017) and Twin Otter (2018) platforms. It operated at a center frequency of 750 MHz with a bandwidth of 300 MHz. MCoRDS3 was flown in 2016 and 2018 aboard a DC8 platform. It operated at a center frequency of 195 MHz with a bandwidth of 50 MHz. These bandwidth configurations provide the required vertical range resolution, which is approximately equivalent to or greater than 3 m in a firn column and 2.5 m in a solid-ice layer [17]. We qualitatively estimate this allows ice slabs with minimum thicknesses of 10 m to be manually mapped via the AR and

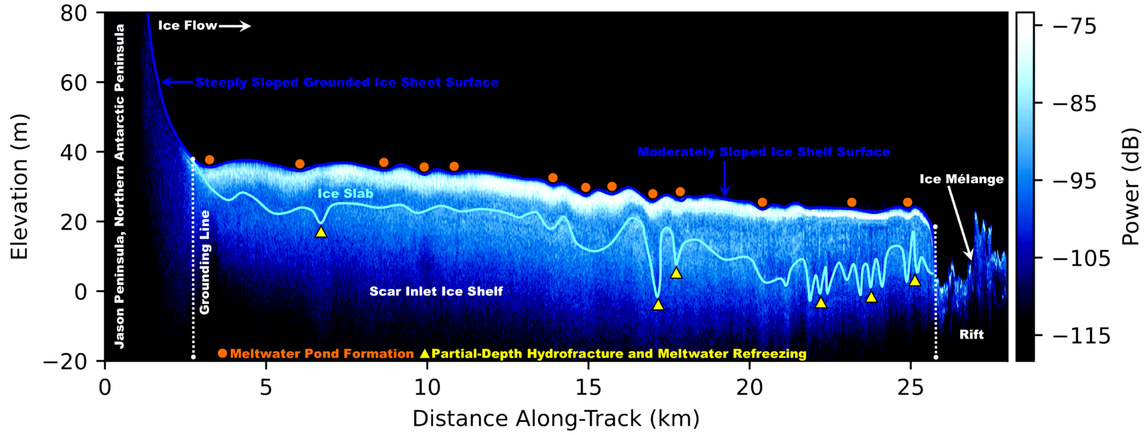

Fig. 2. Example airborne ice-penetrating radar survey collected by AR over Scar Inlet Ice Shelf, Jason Peninsula, northern Antarctic Peninsula, on 31 October 2017 (see Fig. 1 for the location, green star, and Section II-D). The approximately 30 km NASA P3 flight line traverses the steeply sloped grounded ice sheet, the moderately sloped ice shelf, and an ice mélange filled rift. Meltwater pond formation is identified using Landsat high-resolution (30 m) visible satellite imagery (orange circles). The airborne ice-penetrating radar survey shows a ∼10-30 m thick ice slab that is manually mapped via the AR radargram (cyan line, see Section II-D) and suggests partial-depth hydrofracture and meltwater refreezing occur at this location (yellow triangles, see Section IV).

MCoRDS radargrams (e.g., see Fig. 2, cyan line, and see Fig. 1 for the locations, cyan squares). Similar to previous studies, we interpret slightly darker, homogeneous, surface-parallel regions of low reflectivity in the upper firn column (<20 m) as ice slabs [4], [5], [6], [7]. The dielectric contrast between ice slabs and firn layers results in high interface reflectivity. However, limited electromagnetic energy is scattered or absorbed within the ice slabs. It alternately propagates into the deeper firn column and shelf-ice. We validate the manual mapping technique using an AR radargram collected adjacent to the firn cores and GPR transects documented at the field site in Cabinet Inlet (see Fig. 1 for the location, red text) [2].

Coincident with $PC3\Psi_A$, $PC1\Psi_B$, and the mean surface melt days map, we project the manually mapped ice slab locations onto the Southern Hemisphere *EASE-Grid 2.0* at a 3.125 km grid cell spacing. Out of a total of 720,000 grid cells (∼720,000 km^2) that span the mapped percolation facies extent, 1,000 grid cells (∼10,000 km^2) include at least 1 manually mapped ice slab location (<1%). For each of these grid cells, we extract the correlated calibration parameter intervals ($PC3\Psi_A \in [-13, -18]$, $PC1\Psi_B \in [-2, 3]$, and mean surface melt days $\in$ [35, 112]). We respectively attribute low $PC3\Psi_A$ and $PC1\Psi_B$ calibration parameter interval values to Brewster angle effects that occur at smooth dielectric interfaces between ice slabs and firn layers and specular surface scattering that dominates the net backscattering response. A high number of mean surface melt days suggests extensive meltwater infiltration in the upper firn column over time. We apply the calibration parameter intervals to each of the grid cells that span the mapped percolation facies extent. If the extracted values are within these intervals, the grid cell is converted to a binary parameter to map the ice slab extent. Known sources of uncertainty in the calibration technique are described in [5].

III. Results and Discussion

The percolation facies (lighter blue lines) and ice slab (cyan shading) extents mapped via the polarimetric algorithm and the firn aquifer (darker blue shading) extent mapped via the A image time series and the empirically calibrated proof-of-concept polarimetric algorithm described in [20] are shown in Fig. 1. A high-probability ice slab extent of ∼52,000 km^2 is mapped over 23 ice shelves in the Antarctic Peninsula as well as West and East Antarctica—including locations on Seal Nunataks, Scar Inlet, northern Larsen C, George VI, northern Wilkins, Mendelssohn, Bach, Stange, Murphy Inlet, Koether Inlet, Cadwalader Inlet, Holmes, Voyeykov, Moscow University, Totten, Conger, Tracy Tremenchus, Shackleton, West, Publications, Amery, Prince Harald, and Roi Baudouin ice shelves. It is equivalent to 7% of the mapped percolation facies extent and 3% of the mapped Antarctic ice shelf extent (∼1,570,000 km^2). A fully validated firn aquifer extent of ∼9,000 km^2 is mapped over 3 ice shelves in the Antarctica Peninsula—including comparatively high snow accumulation locations on Müller, northern George VI, and Wilkins ice shelves. It is equivalent to 1% of the mapped percolation facies extent and 0.6% of the mapped Antarctic ice shelf extent. As demonstrated in Greenland [4], [5], these distinct, but related, sub-facies of the percolation facies are defined by differences in snow accumulation, which influences the englacial ice shelf hydrology and thermal characteristics of the firn column.

We attribute ice slab formation to: (1) intense surface melting and possibly heavy rainfall events leading to wetting front propagation and preferential flow [8], [9], [12] and (2) enhanced surface melting driven by episodic föehn and katabatic winds [27], especially in grounding zones where the steeply sloped grounded ice sheet is channeled downslope into the moderately sloped ice shelf by the topography (e.g., see Fig. 2, blue line). These mechanisms result in localized vertical and heterogeneous meltwater infiltration and lateral flow along hydraulic pathways that refreezes in the upper firn column (e.g., see Fig. 2, cyan line). Ice slabs are correlated with expansive clusters of ice dolines (see Fig. 1 for the locations, yellow triangles)—defined as meltwater-induced collapse features that span spatial scales of hundreds of square meters and have depths of tens of meters beneath the surface [28].

IV. Conclusions and Future Work

The results of this exploratory study are a first demonstration of the capability for mapping the previously unidentified ice slab extent over the percolation facies of Antarctic ice shelves from space using quad-polarimetric, L-band satellite radar scatterometry. Although the σ^o observations collected by the short-lived radar aboard the SMAP mission [16] represent only a brief snapshot in time, they provide a novel testbed for proof-of-concept polarimetric algorithm development relevant to the ESA P-band Biomass mission [29] launched in late 2025, the forthcoming ESA Radar Observation System for Europe in L-band (ROSE-L) mission [30] expected to be launched in 2028, and the NASA-proposed Global L-band Observatory for Water Cycle Studies (GLOWS) mission [31].

The launch of innovative, quad-polarimetric, low-frequency (L- and P-band) satellite SAR missions that collect σ^o observations at high-resolution (meters) on decadal timescales and the development of sophisticated polarimetric algorithms that use advanced multivariate statistical or deep learning techniques can generate maps of the ice slab extent with an effective resolution up to three orders of magnitude greater than those demonstrated in this exploratory study. These maps can be used to: (1) quantify interannual variability in the ice slab extent and, critically, (2) track widespread ice slab formation and expansion that can lead to widespread meltwater pond formation. Meltwater ponds can drive partial-depth hydrofracture into the shelf-ice (e.g., see Fig. 2, orange circles and yellow triangles) as well as rapid, full-shelf-ice-thickness hydrofracture and ocean drainage through ice dolines [28], [32], [33]. Repeated filling and draining of meltwater ponds can trigger loading-induced flexure and shallow, intersecting, ring fracture [33] followed by explosive, chain reaction hydrofracture and catastrophic Antarctic ice shelf disintegration [32].

Acknowledgment

CReSIS data was generated with support from University of Kansas, NASA OIB (NNX16AH54G), NSF (ACI-1443054, OPP-1739003, IIS-1838230), Lilly Endowment Inc., and Indiana METACyt Initiative. We thank A. Luckman for the Antarctic ice shelf mean surface melting days map. All generated data is available at: https://doi.org/10.5281/zenodo.20370861.

References

[1] C. S. Benson, "Stratigraphic studies in the snow and firn of the Greenland ice sheet," Ph.D. dissertation, California Institute of Technology, 1960.

[2] B. Hubbard, A. Luckman, D. W. Ashmore *et al.*, "Massive subsurface ice formed by refreezing of ice-shelf melt ponds," *Nat. Comm.*, vol. 7, no. 1, p. 11897, 2016.

[3] H. Machguth, M. MacFerrin, D. van As *et al.*, "Greenland meltwater storage in firn limited by near-surface ice formation," *Nat. Clim. Change*, vol. 6, no. 4, pp. 390–393, 2016.

[4] M. MacFerrin, H. Machguth, D. v. As, Charalampidis *et al.*, "Rapid expansion of Greenland's low-permeability ice slabs," *Nat.*, vol. 573, no. 7774, pp. 403–407, 2019.

[5] J. Z. Miller, R. Culberg, D. G. Long *et al.*, "An empirical algorithm to map perennial firn aquifers and ice slabs within the Greenland ice sheet using satellite L-band microwave radiometry," *Cryosphere*, vol. 16, no. 1, pp. 103–125, 2022a.

[6] N. Jullien, A. J. Tedstone, H. Machguth *et al.*, "Greenland ice sheet ice slab expansion and thickening," *Geophys. Res. Lett.*, vol. 50, no. 10, p. e2022GL100911, 2023.

[7] R. Culberg, R. J. Michaelides, and J. Z. Miller, "Sentinel-1 detection of ice slabs on the Greenland ice sheet," *Cryosphere*, vol. 18, no. 5, pp. 2531–2555, 2024.

[8] J. Harper, N. Humphrey, W. T. Pfeffer *et al.*, "Greenland ice-sheet contribution to sea-level rise buffered by meltwater storage in firn," *Nat.*, vol. 491, no. 7423, pp. 240–243, 2012.

[9] N. F. Humphrey, J. T. Harper, and W. T. Pfeffer, "Thermal tracking of meltwater retention in Greenland's accumulation area," *J. Geophys. Res.: Earth Surf.*, vol. 117, no. F1, 2012.

[10] J. E. Box, A. Wehrlé, D. van As *et al.*, "Greenland ice sheet rainfall, heat, and albedo feedback impacts from the mid-August 2021 atmospheric river," *Geophys. Res. Lett.*, vol. 49, no. 11, p. e2021GL097356, 2022.

[11] S. V. Nghiem, D. K. Hall, T. L. Mote *et al.*, "Extreme melt across the Greenland ice sheet in 2012," *Geophys. Res. Lett.*, vol. 39, no. 20, 2012.

[12] J. Harper, J. Saito, and N. Humphrey, "Cold season rain event has impact on Greenland's firn layer comparable to entire summer melt season," *Geophys. Res. Lett.*, vol. 50, no. 14, p. e2023GL103654, 2023.

[13] A. Tedstone, H. Machguth, N. Clerx *et al.*, "Concurrent superimposed ice formation and meltwater runoff on Greenland's ice slabs," *Nat. Comm.*, vol. 16, no. 1, p. 4494, 2025.

[14] F. T. Ulaby and D. G. Long, *Microwave Radar and Radiometric Remote Sensing*. Ann Arbor, Michigan, USA: Univ. Michigan Press, 2014.

[15] D. G. Long and J. Z. Miller, "Validation of the effective resolution of SMAP enhanced resolution backscatter products," *IEEE J. Sel. Topics App. Earth Obs. Rem. Sens.*, vol. 16, pp. 3390–3404, 2023.

[16] D. Entekhabi, E. G. Njoku, P. E. O'neill *et al.*, "The Soil Moisture Active Passive mission," *Proc. IEEE*, vol. 98, no. 5, pp. 704–716, 2010.

[17] F. Rodriguez-Morales, S. Gogineni, C. J. Leuschen *et al.*, "Advanced multifrequency radar instrumentation for polar research," *IEEE Trans. Geosci. Rem. Sens.*, vol. 52, no. 5, pp. 2824–2842, 2014.

[18] S. L. Bevan, A. J. Luckman, P. Kuipers Munneke *et al.*, "Decline in surface melt duration on Larsen C Ice Shelf revealed by the Advanced Scatterometer)," *Earth Space Sci.*, vol. 5, no. 10, pp. 578–591, 2018.

[19] R. D. Lindsley and D. G. Long, "Enhanced-resolution reconstruction of ASCAT backscatter measurements," *IEEE Trans. Geosci. Rem. Sens.*, vol. 54, no. 5, pp. 2589–2601, 2016.

[20] J. Z. Miller, D. G. Long, C. A. Shuman *et al.*, "Satellite mapping of the extent and physical characteristics of an expansive firn aquifer in Wilkins Ice Shelf, Antarctic Peninsula," in *IGARSS 2023*, 2023, pp. 219–222.

[21] T. A. Scambos, T. M. Haran, M. A. Fahnestock *et al.*, "MODIS-based Mosaic of Antarctica (MOA) data sets: Continent-wide surface morphology and snow grain size," *Rem. Sens. Envir.*, vol. 111, no. 2-3, pp. 242–257, 2007.

[22] D. G. Long and M. R. Drinkwater, "Azimuth variation in microwave scatterometer and radiometer data over Antarctica," *IEEE Trans. Geosci. Rem. Sens.*, vol. 38, no. 4, pp. 1857–1870, 2000.

[23] ——, "Greenland ice-sheet surface properties observed by the Seasat-A scatterometer at enhanced resolution," *J. Glaciology*, vol. 40, no. 135, p. 213–230, 1994.

[24] M. R. Drinkwater, D. G. Long, and A. W. Bingham, "Greenland snow accumulation estimates from satellite radar scatterometer data," *J. Geophys. Res.: Atm.*, vol. 106, no. D24, pp. 33 935–33 950, 2001.

[25] C. Shuman, T. Scambos, and E. Berthier, "Ice loss processes in the Seal Nunataks Ice Shelf region from satellite altimetry and imagery," *Ann. Glaciology*, vol. 57, no. 73, pp. 94–104, 2016.

[26] E. Rignot, "Backscatter model for the unusual radar properties of the Greenland Ice Sheet," *J. Geophys. Res. Planets*, vol. 100, no. E5, pp. 9389–9400, 1995.

[27] M. K. Laffin, C. S. Zender, M. van Wessem *et al.*, "Wind-associated melt trends and contrasts between the Greenland and Antarctic ice sheets," *Geophysical Research Letters*, vol. 50, no. 16, p. e2023GL102828, 2023.

[28] R. Bindschadler, T. A. Scambos, H. Rott *et al.*, "Ice dolines on Larsen Ice Shelf, Antarctica," *Ann. Glaciol.*, vol. 34, pp. 283–290, 2002.

[29] S. Quegan, T. Le Toan, J. Chave *et al.*, "The European Space Agency Biomass mission: Measuring forest above-ground biomass from space," *Remote Sens. Environ.*, vol. 227, pp. 44–60, 2019.

[30] M. W. Davidson and R. Furnell, "ROSE-L: Copernicus L-band SAR mission," in *IGARSS 2021*, 2021, pp. 872–873.

[31] D. Long, R. Bindlish, J. Piepmeier *et al.*, "Global L-band Observatory for Water Cycle Studies (GLOWS)," in *IGARSS 2021*, 2021, pp. 7779–7782.

[32] A. F. Banwell, D. R. MacAyeal, and O. V. Sergienko, "Breakup of the Larsen B Ice Shelf triggered by chain reaction drainage of supraglacial lakes," *Geophys. Res. Lett.*, vol. 40, no. 22, pp. 5872–5876, 2013.

[33] A. F. Banwell, I. C. Willis, L. Stevens *et al.*, "Observed meltwater-induced flexure and fracture at a doline on George VI Ice Shelf, Antarctica," *J. Glaciol.*, vol. 70, p. e47, 2024.